PAPER

Check for updates

Entropically controlled assemblies of conjugated amphiphiles

Xiangyu Zhang and Thi Vo ![ORCID] *

Amphiphiles with conjugated subunits possess favorable optical and electronic properties as well as the intrinsic ability to propagate these features across scales *via* supramolecular self-assembly. These capabilities highlight their tremendous potential for applications in drug delivery, sensing, flexible electronics, and/or integrated circuits. However, achieving systematic control over their self-assembled morphologies remains challenging due to the lack of understanding on how the effects of molecular geometry propagate across hierarchical length scales to influence their mesoscale assembly behaviors. Herein, we employ a combination of molecular dynamics simulations and a scaling theory to characterize the assembly behaviors for a model system of conjugated amphiphiles. Firstly, we demonstrate how variations in the length of each amphiphilic block modulate its equilibrium supramolecular self-assembly behaviors using a coarse-grained simulation model that preserves the intrinsic molecular-level geometries of each respective conjugated motif. Then, we employ a scaling theory to elucidate the microscopic interactions driving the observed morphological shifts in simulations. Our findings reveal that the supramolecular self-assembly of conjugated amphiphiles is governed by a balance between association enthalpy arising from $\pi-\pi$ interactions and entropic penalties arising from geometry-mediated steric repulsions. Then, we leveraged the insights provided by simulation and theory to predict a suite of self-assembled morphologies accessible using our model amphiphilic system across experimentally testable design parameters. Our findings not only establish a practical approach to simulate the mesoscale self-assembly of conjugated amphiphiles but also provide important insights into the microscopic mechanisms underlying their macroscopic behaviors.

I. Introduction

Recent advances in synthesis and supramolecular self-assembly have led to an unprecedented growth in our ability to create synthetic materials exhibiting a diverse range of complex architectures.[1–13] These features can include different monomer chemistries that introduce novel properties into existing polymers, thereby creating multifunctional materials,[4,14–23] or sequence-controlled oligomeric sequences that direct hierarchical organizations during processing/assembly.[4,24–29] Amongst this expansive library of materials, conjugated moieties have emerged as an attractive suite of molecular chemistries owing to their strong optical, electronic, and biological properties, which make them amenable for applications in flexible displays,[30] integrated circuits,[31] sensors,[32] smart e-skins,[33] wearable electronics,[34–38] and drug delivery.[39,40]

One popular class of synthetic materials constructed from conjugated moieties is π-conjugated amphiphiles.[7,14–16,41–46] Although each specific amphiphile can differ, the key design paradigm for synthesizing conjugated amphiphiles and their

Chemical and Biomolecular Engineering, Johns Hopkins University, Baltimore, MD 21218, USA. E-mail: tvo12@jhu.edu

subsequent self-assembly centers around combining two types of oligomeric blocks, *i.e.*, a flexible (non-conjugated, amorphous) block and a conjugated block. Specifically, the flexible blocks regulate self-assembly *via* noncovalent associative interactions and/or steric stabilization/limitation, while the conjugated blocks direct additional ordering within the micro-separated, conjugated domains *via* quadrupolar and $\pi-\pi$ interactions. This latter feature of emergent orientational and structural ordering within a sub-domain makes π-conjugated amphiphiles particularly useful in supramolecular and hierarchical self-assembly. For example, π-conjugated peptide amphiphiles have been shown to organize into nanofibers/networks of co-facial $\pi-\pi$ ring stacking, thereby mediating charge transport for organic electronics applications.[5,47,48] Alternatively, π-conjugated drug molecules can be covalently linked to an OEG-bottlebrush tail to drive their self-assembly into nanostructured micelles with tightly aligned $\pi-\pi$ packing inside their core.[39] This additional $\pi-\pi$ alignment increases the spectroscopic responses of the conjugated molecules, providing an alternative handle for the imaging and detection of therapeutics.[49,50]

Despite their tremendous potential, systematic control over the spatial and orientational ordering of the conjugated domain during supramolecular self-assembly remains an on-going

challenge. Unlike their flexible counterparts, conjugated monomers are more rigid and possess well-defined anisotropic geometries. Consequently, the interplay between enthalpic effects such as π–π stacking and entropic effects arising from geometrical packing can disrupt the desired, pre-programmed morphological ordering embedded into the molecular structure of the amphiphile.[51–54] Efforts to address this challenge have leveraged atomistic simulations to characterize the precise orientational and spatial ordering between the conjugated monomers at a local level.[5,41,43,55,56] However, these models are often very complex, making it computationally prohibitive to simulate mesoscale assembehaviors for direct comparison with experimental observations. Alternatively, although coarse-grained methods have been developed to simulate conjugated interactions,[57,58] the typical approaches utilize spherical monomers to model parts (or an entire) of the conjugate monomer. These simplifications ignore the geometrical constraints imposed by the shape of the conjugate monomers and cannot accurately trace how the effect of molecular geometry propagates across scales to influence the experimentally observed morphologies. This lack of insight limits our current abilities to *a priori* tune the emergent shapes, sizes, and hierarchical ordering of conjugated amphiphiles during supramolecular self-assembly.

In this study, we address this open question using a coarse-grained model designed to preserve the molecular geometry, which is also computationally inexpensive, to enable the characterization of mesoscale assembly behaviors. Specifically, we preserve the geometrical fidelity of the conjugated monomers by simulating them as anisotropic monomers whose shape reflects the molecular structure of the monomer. The, we explore the mesoscale assembly behaviors of a model system of triblock flexible-conjugated-flexible amphiphiles across two amphiphile design handles commonly varied in experiments, *i.e.*, flexible block length and conjugate block length. To explain the physical origins of the observed morphologies, we developed a scaling theory that balances the enthalpic gain from π–π stacking against the entropic loss due to crowding between the flexible blocks. Our results highlight a critical interplay between the conjugated and flexible blocks that produces a diverse suite of self-assembled structures spanning filaments, networks, and self-limiting clusters, all of which exhibit spatially and orientationally ordered stackings between the conjugated monomers known from experiments and atomistic simulations.[56] Thus, our combined theory and simulation framework provides a powerful tool to guide the design of conjugated amphiphiles spanning a range of experimentally relevant handles such as block lengths, amphiphile architectures, and monomer geometries.

II. Methods

Computational model

We first present our coarse-grained simulation model for the triblock flexible-conjugated-flexible amphiphiles of interest. Fig. 1a illustrates the mapping between the molecular structure
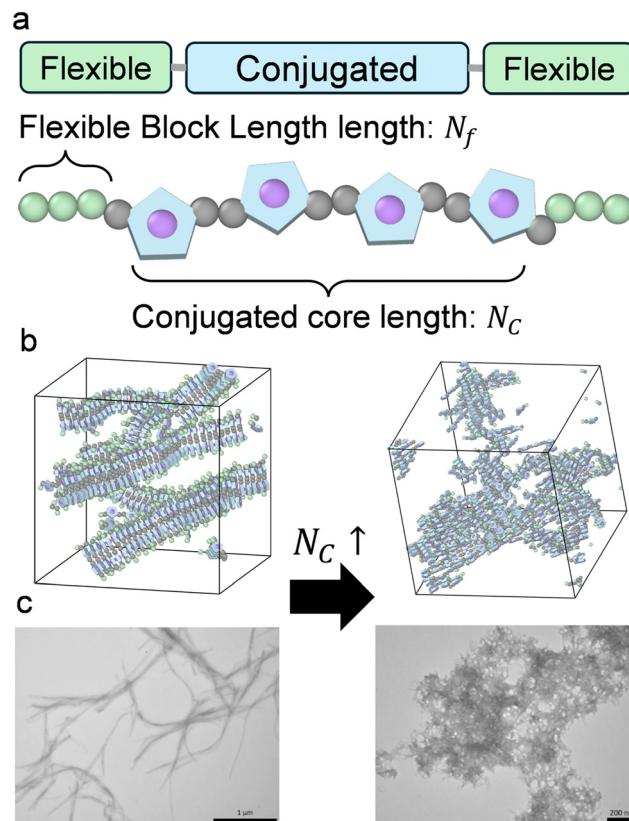
Fig. 1 Simulation of conjugated amphiphiles. (a) Schematic of the mapping between molecular structure and the coarse-grained model. Conjugated beads are modelled as pentagonal prisms to preserve their respective molecular geometry. All other beads utilize a spherical monomer geometry. Specifically, in this schematic, N_f = 3 and N_c = 4. (b) Simulation snapshots showing the transitions from a filament to network structures with an increase in the conjugated block (N_c) length, reproducing (c) experimentally observed behaviors. Panel (c) is reproduced with permission from ACS Publications.[70]

of the amphiphile and the model. Specifically, we place the conjugated block at the center and flexible blocks flanking the left and right ends of the amphiphile. We select a pentagonal geometry (pentagonal prism) for the conjugated monomers to model the geometry of thiophene, a common monomer used in the synthesis of conjugated amphiphiles.[45,46,56,59] The thickness and edge length of the pentagonal prism used to model thiophene were selected to match the average ratio between the π–π stacking distance (d_π) and C–C bond length (d_C) for thiophene,[60] where $d_\pi/d_C \sim 2.5$. To simulate the anisotropic particle geometries, the interactions between the pentagonal prisms utilize the anisotropic Lennard-Jones potential (ALJ).[61] Given that bonding between the conjugated monomers is site specific, we utilize a spherical bonding site (Fig. 1a, gray beads) to mediate the connectivity between the thiophene monomers. The size of this spherical bonding site is set to be the same as the monomer size for the flexible block and defined to be 0.6–0 times the edge length of the pentagonal prism to match the ratio between the peptide and C–S bond length within the conjugated thiophene ring.[60] To capture the relevant π–π stacking between the

conjugated monomers, we employ a dipole–dipole interaction potential, with the dipole moment defined to be perpendicular to the large face of the pentagonal prism (in the particle frame). Additionally, we include a central bead to induce tilted stacking between the conjugated monomers (Fig. 1a, purple beads). Combined, this set of interaction potentials preserves the offset π–π stacking observed in experiments and atomistic simulations.[45,46,56,59] All other interactions are set to be sterically repulsive *via* the Weeks–Chandler–Anderson (WCA) potential.[62] All bonding between conjugated and flexible monomers utilizes the finite extensible nonlinear elastic (FENE) potential[63] to reproduce the self-avoiding, flexible nature of the non-conjugated amphiphile monomers. Lastly, we use both a harmonic angle potential and an OPLE dihedral potential[64] to constrain the rotations between the conjugated monomers. This was specifically constructed to reflect the rigidity observed in both experiments and atomistic simulations.[5,43,55] Simulations performed using our proposed model can reproduce both the filament and network mesoscale structures observed in experiments with increasing conjugated block lengths (Fig. 1b and c). Full details of the simulation model, including all relevant potential parameters, are presented in Appendix A in the SI.

To elucidate the mechanisms underpinning how a flexible block length (N_f) and conjugate block length (N_c) impact the self-assembly of amphiphiles, we vary N_f from 1 to 25 and N_c from 1 to 4. These lengths are selected for comparison with experimentally synthesized amphiphiles in the literature.[56] All simulations are performed using HOOMD-blue[65] under the canonical ensemble (NVT) using the Nose Hoover thermostat[66] with reduced units of $T^* = 1$ and integration timestep of 0.002. In our simulations, solvent effects are implicitly accounted for *via* the relative differences in the pairwise interaction energy between particles. Specifically, we defined the interaction parameters to produce steric repulsion interactions between the monomers in the flexible blocks and dipole-mediated attractions between the monomers in the conjugated blocks. In this way, the dipole-mediate interactions mimic the poor solvent conditions between the conjugated cores, thereby driving self-assembly. Similarly, the steric-mediated repulsion between the flexible blocks mimics the solvation shells around the flexible monomers (*i.e.* good solvent), which arise in explicit solvent systems that prevent aggregation. Each simulation contains 160 amphiphiles at a set volume fraction of 0.02. To maintain this target volume fraction, the simulation box is varied in size. Larger systems (longer N_c or N_f) will have larger box sizes, but all simulation boxes are scaled to ensure a constant system volume fraction across the entire suite of simulations performed. All simulations were run for a minimum of 8×10^7 integration time steps. To ensure that the self-assembled morphology is the equilibrium structure, we additionally perform extensive simulated thermal annealing, where the simulation temperature undergoes extensive cyclical thermal oscillation. In each cycle, the system is heated to a high temperature of $T^* = 1.2$ and allowed to adapt to the new temperature for 1×10^6 integration timesteps. This is followed by lowering the temperature to $T^* = 1.0$ and equilibration for 4×10^6 integration timesteps to allow the reassembly of the melted local defects.

Order parameters

We anticipate that the amphiphiles will self-assemble into core–shell like structures, where their core contains the π–π stacked conjugated monomers and the flexible monomer makes up the corona (shell). Therefore, to characterize the morphology of the self-assembled amphiphiles in our simulations, we employ two order parameters, α (eqn (1)) and ϕ (eqn (2)). Mathematically, α is defined as follows:

$$\alpha = \sum_i \left(\frac{\alpha_i}{n_T} \right)^2 \tag{1}$$

where n_T is the total number of amphiphiles in the simulation and α_i is the number of amphiphiles within a self-assembled structure (cluster). The summation runs over all distinct clusters observed in the equilibrated system. Clusters are identified by grouping all conjugated monomers whose center-to-center distances fall within 1.5 times the size of the central bead (purple particles, Fig. 1a). This tight cutoff is set to ensure that only conjugated monomers that directly contact each other are clustered together. Physically, α represents a scaled aggregation number (between $1/n_T$ and 1) for the self-assembled structure observed in the simulations. When α approaches 1, all amphiphile chains are connected into one continuous network. Conversely, $\alpha = 1/n_T$ indicates that every amphiphile is in its own cluster, which correlates to a disordered system.

To quantify the alignment between conjugated monomers, we first note that the associations between the pentagonal prisms are mediated by face-centered dipole–dipole interactions. This means that monomers can only stack face-to-face relative to each other. Consequently, an angle cutoff will yield the same relative angle between monomers, making it difficult to use it as an order parameter for characterization. For this reason, we introduce the parameter ϕ, which is defined as follows:

$$\phi = \frac{1}{N_c} \sum_i \left(\frac{\phi_i}{n_T} \right)^2 \tag{2}$$

where ϕ_i is the number of conjugated monomers stacked on top of each other within a cluster and the summation is again taken over all clusters observed in the simulations. By construction, ϕ provides a scaled metric (between $1/n_T$ and 1) for the extent of face-to-face stacking between the conjugated monomers, normalized by the number of conjugated monomers per amphiphile. A decrease in ϕ indicates more misalignment between the conjugate blocks and $\phi = 1/n_T$ means that the conjugated blocks are orientationally disordered. This convergence to $\phi = 1/n_T$, as opposed to 0 for no alignment, reflects our definition of counting a free, unassociated conjugated monomer to contribute to 1 face-to-face stacking within the clusters. Additionally, ϕ can never exceed α, given that the number of stacked conjugated blocks is constrained by the aggregation number of the cluster. Through this lens, ϕ provides information about the morphology of the self-assembled structure. A low ϕ indicates disordered/no assembly, while a high ϕ suggests filament-like structures. We provide two clarifying examples for the behavior of ϕ, *i.e.*, quantification for a misaligned and perfectly aligned structure in Fig. 2 for the

Misaligned Stacking
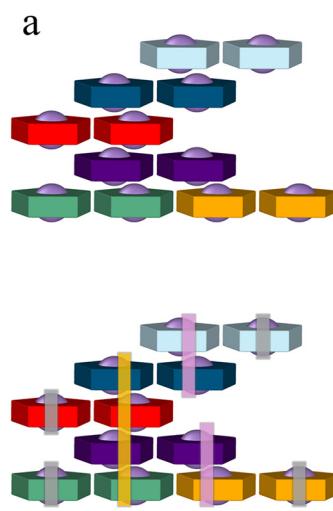
Aligned Stacking
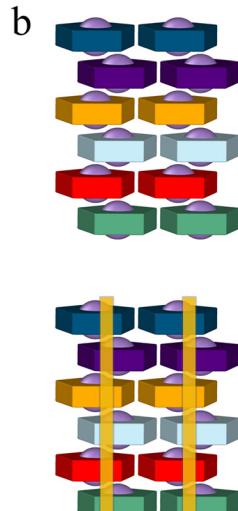
Fig. 2 Alignment order parameter. (a) Misaligned stacking example (ϕ = 0.39) and (b) perfect stacking example (ϕ = 1.0). For each, top row shows the structure. Bottom row draws lines connecting the different face-to-face motifs. In (a), the gray line (4 total) identifies the motif with only 1 monomer, pink (2 total) identifies the motifs with 2 face-to-face aligned monomers, and the yellow line (1 total) shows the motif with 4 face-to-face aligned monomers. In (b), the yellow line (2 total) highlights the motif with 6 face-to-face aligned monomers.

case of $N_c = 2$. Fig. 2a (top) shows a "misaligned" stacking in a system with a total of 6 amphiphiles, individually colored for clarity, where each amphiphile has 2 conjugate monomers (two per color). By inspection, there are 3 stacking motifs (Fig. 2a, bottom). The first corresponds to the 4 monomers (gray line) with

no face-to-face stacking with any other monomers. The second corresponds to 2 subsets of particles (pink line) each with 2 monomers showing face-to-face stacking. The last corresponds to 1 subset of particles (yellow line) with 4 monomers exhibiting continuous face-to-face stacking. The definition of ϕ (eqn (2)) is as follows: $\phi = \frac{1}{2}\left[4\left(\frac{1}{6}\right)^2 + 2\left(\frac{2}{6}\right)^2 + \left(\frac{4}{6}\right)^2\right] = \frac{7}{18}$. This value corresponds to a limit of low alignment between the conjugated monomers. Conversely, Fig. 2b (top) shows the same 6-amphiphile system but with a "perfectly aligned" configuration between the conjugated monomers. Here, there is only 1 motif, *i.e.*, 6 monomers with continuous face-to-face stacking (yellow line in Fig. 2b, bottom). Given that there are two instances of this motif, $\phi = \frac{1}{2}\left[2\left(\frac{6}{6}\right)^2\right] = 1$. More detailed example calculations for both α and ϕ for other relevant morphologies are shown in Appendix B, Fig. B1. Parameters α and ϕ will be used to analyze and categorize the morphologies observed from simulations.

III. Results and discussion

Order parameter and morphology characterization

We first compute the distributions of individual components in our defined order parameters (eqn (1) and (2)) to gain insights into the types of self-assembled morphologies observed. More specifically, we characterize the distributions of α_i and ϕ_j across all clusters observed within a given simulation during the assembly production run. For ease of discussion, we normalize the x-axis for the subsequent distribution plots (Fig. 3a–d) by the total number of amphiphiles (n_T). Analysis of the results show four major features in their respective behaviors.
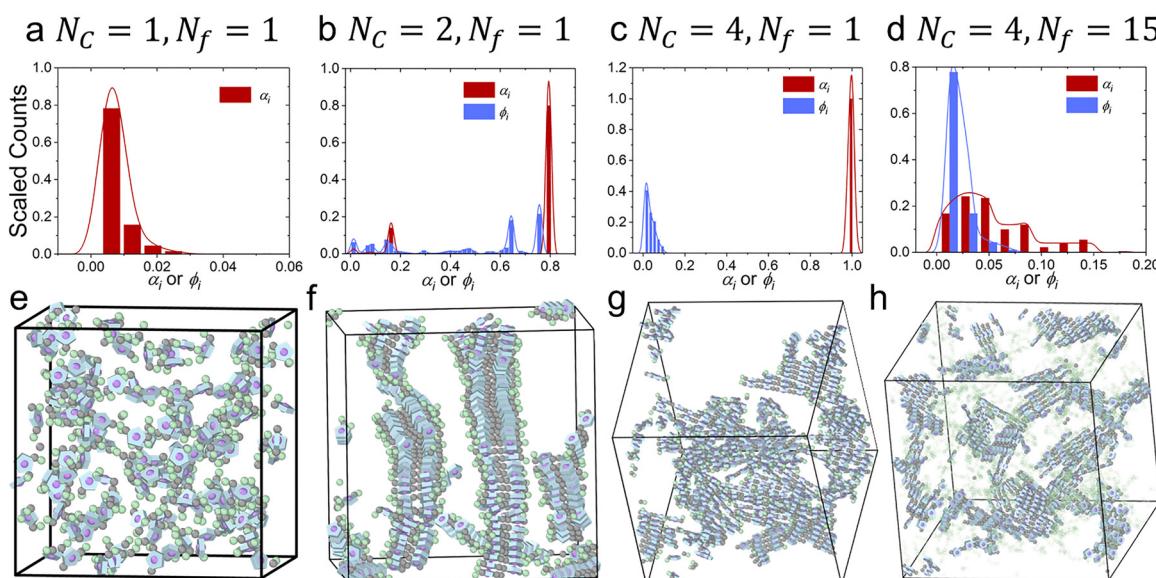
Fig. 3 Order parameter characterization of self-assembled morphologies. Distribution of α (eqn (1)) and ϕ (eqn (2)) for the following systems: (a) $N_c = 1$, $N_f = 1$ (ϕ_i distribution is identical to α_i); (b) $N_c = 2$, $N_f = 1$; (c) $N_c = 4$, $N_f = 1$; and (d) $N_c = 4$, $N_f = 15$. For each distribution, the x-axis is the scaled number of chains in the cluster and y-axis is the scaled counts for the observed cluster. (e)–(h) Display the corresponding simulation snapshots for distributions in (a)–(d), respectively. From left to right [panels (a)–(d)], we classify the morphology as no-assembly, filament, network, and self-limiting, respectively.

The first feature indicates a dominant peak near $1/n_T$ for both α_i and ϕ_i (Fig. 3a). Here, α_i is identical to the ϕ_i distribution because there is only one conjugated core per chain. This feature indicates that each cluster only contains one amphiphile. This distribution highly indicates an unassociated (*i.e.* no assembly) configuration between the amphiphiles. Indeed, visualization of the simulation reveals that the amphiphiles remain dispersed (Fig. 3e). The second feature observed shows a peak in both α_i and ϕ_i, which are close to 1 (Fig. 3b). This suggests that almost all the amphiphiles belong to a single cluster and the conjugated blocks within the cluster are perfectly stacked relative to each other without significant misalignments. These features correspond to linear, filament-like motifs, which we further confirm by visualization of the self-assembled structure from simulation (Fig. 3f). We note in Fig. 3f by visual inspection that there appears to be multiple filaments as opposed to long system spanning filaments. This is an artifact of the periodic boundary conditions, where the filaments are connected across the periodic boundary of the simulation box. Fig. C5 (Appendix C) in the SI redraws the filaments in Fig. 3f replicated along their periodic boundaries to provide a clearer picture of how multiple filaments are all connected into one long, system spanning structure. The third feature also exhibits a high peak in α_i near 1 but a significantly lower peak location for ϕ_i, which is around 0.01 (Fig. 3c). This implies that nearly all the amphiphiles belong to a single cluster, but the conjugated cores have high stacking misalignments. Combined, both features suggest that the amphiphiles are highly associated but grow in multiple directions (as opposed to the filament limit). These motifs are intrinsic to network-like structures, as shown in the corresponding simulation snapshot (Fig. 3g). The last feature exhibits a broad peak at small α_i, while ϕ_i gives a dominant peak close to 0 (Fig. 3d). This suggests that the amphiphiles aggregate into small clusters with a large degree of misaligned conjugated blocks. These intermediate values across both α_i and ϕ_i also suggest the formation of self-limiting clusters, which is further validated by visualization of the simulation results (Fig. 3h). Additional simulation snapshots across all the studied systems are reported in Appendix C of the SI. We note that a tail exists in the α distribution for the self-limiting structure shown in Fig. 3d. To resolve this feature, we perform additional thermal annealing for an extra 8×10^7 simulation timesteps to push the system further into the thermodynamic limit. The measured distribution becomes more continuous, but the tail remains. Further inspection of the range of α values indicates that the differences correspond to fluctuations between approximately 5 amphiphiles per cluster across all clusters observed in the simulations. Therefore, we associate these results with the fluctuations in the self-limiting behaviors that arise from free amphiphiles attempting to add to the growing filament, and subsequently ejected due to the strong steric constraints imposed by the flexible blocks.

Amongst the observed morphologies, the most interesting is the self-limiting clusters (Fig. 3h), which suggests the presence of a mechanism that limits cluster growth. We posit that this mechanism is entropically controlled and associated with chain crowding. Phenomenologically, each amphiphile added to the growing cluster must balance two opposing effects, as follows: (1) enthalpic gain from interactions between the conjugated blocks and (2) entropic loss from the increased crowding between the flexible blocks. In other words, each new monomer adds favorable π–π interactions but also increases the steric repulsion between other monomers already present. Eventually, this steric build-up exceeds the enthalpic gain, thereby terminating the assembly process. More specifically, when the energy needed to compress chains at the growing front exceeds that afforded by the incorporation of an additional amphiphile, the filament will stop growing. A schematic summarizing this process is shown in Fig. 4a.

Conjugated amphiphile self-assembly scaling theory

Here, we present a scaling theory that aims to capture the above-mentioned phenomenological picture. From the perspective of chain crowding, polymer corona predictions for anisotropic particles provide a convenient starting point for the quantification of the chain energetics.[51,67–69] This is because the core formed *via* the conjugated blocks pins one end of the flexible block to the surface of the core, effectively making it behave akin to a functionalized chain anchored to an anisotropic core. More specifically, we recognize that our self-assembling amphiphiles form filament-like structures. Accordingly, the geometry of the growing core can be approximated as that of a cylinder with a constant radius but grows in length as the number of aggregated amphiphiles increases (Fig. 4a). To set the stage for our theoretical development, it is worthwhile to recap the key features for predicting the corona morphologies on anisotropic particles. Briefly, traditional theories predict the size of the polymer corona (R) using a packing argument, where polymers preferentially partition to surface locations on the core particle, which reduce the steric confinement with neighboring chains.[51,67–69] Therefore, a key feature of brush theories aims to predict the monomer density profile (ρ) as a function of the distance (r) away from the particle surface. In the case of a long chain length, the monomer density profile has the form $\rho(r) \sim \Omega^{-2}\nu^{-1/3}\alpha^{2/3}(rb^{-1})^{-4/3}$, where ν is the excluded volume of each monomer, α is the number of chains, b is the Kuhn length, and Ω is a shape parameter. Excluded volume (ν) is also often defined with respect to the Kuhn length (b), as follows:[51,67] $\nu \sim b^3$. We note here that the number of chains is linearly proportional to the aggregation number of the self-assembled structure given that each amphiphile brings 2 flexible blocks to the core, motivating the usage of the same variable α. Geometrically, the shape parameter Ω defines the distance from the surface of the growing cylinder, normalized by its insphere radius. Here, Ω is a function of the azimuthal and polar angles and maps the surface of the cylinder, as shown in Fig. 4b. Mathematically, for the ith point on the particle surface, Ω_i is defined as follows:

$$\Omega_i(\theta, \psi) = \frac{\|r_i(\theta, \psi) - r_0\|}{\min(\{\|r_i(\theta, \psi) - r_0\|\})} \qquad (3)$$
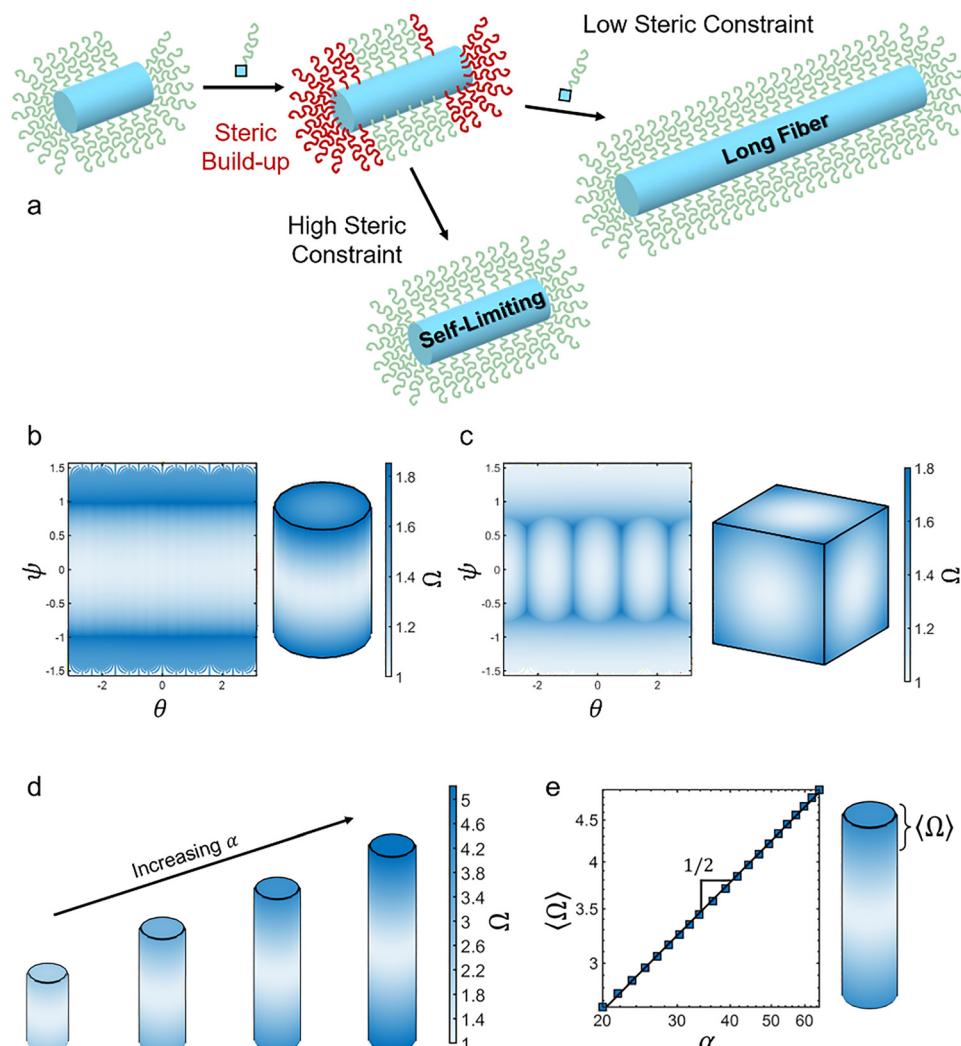
Fig. 4 Scaling theory development of self-limiting amphiphile behaviors. (a) Schematic of the growth behavior of conjugated amphiphiles, where high steric repulsions limit the emergent size of the supramolecular assemblies. Mapping of azimuthal (θ) and polar (ψ) angles on the surface of a (b) cylinder and (c) cube, showing the associated Ω values. (d) Dependence of Ω value on cylinder height, which corresponds to increasing aggregation number α. (e) Scaling behaviour of the Ω value at the cylinder ends as a function of the cylinder heights.

where $r_i(\theta,\psi)$ is the position on the particle surface, r_0 is the center of mass of the particle, and the denominator represents the smallest of the set of $\|r_i - r_0\|$ values for all points on the particle surface. The definition of Ω is generalized for all anisotropic particle geometries, and thus there is no analytical form. In practice, Ω_i is computed by first constrting a surface mesh for the shape of interest, and then evaluating eqn (3) at all surface mesh points. For clarity, a secondary example of Ω parameterization for the surface of a cube is also shown in Fig. 4c. Knowledge of $\rho(r)$ then enables predictions of the corona size at a given surface location, $R(\Omega)$, using the volumetric balance $N\alpha b^3 \sim \int_0^{R(\Omega)} \rho(r)\Omega^3 r^2 \mathrm{d}r$, where N is the polymer chain length. Physically, this approach leverages knowledge of monomer packing to determine the effective space that the chain will take up at a given surface location on the anisotropic core. In other words, it maps the degree of chain crowding to an emergent corona size, which enables direct quantification of the steric repulsion energy cost (F_s) between neighboring chain

as $F_s \sim \nu\alpha N^2 R^{-3}$. For this reason, applying corona prediction to our amphiphile system serves as a natural way to quantify the interplay between entropy and enthalpy in directing amphiphile self-assembly.

However, current theories assume a constant grafting surface/core geometry and large chain lengths, and both assumptions place them outside the limit of applicability for our system. To address the limitations associated with the core geometry, we note that increasing the aggregation number (α) of the cylinder augments Ω at the growing front. This is because as the cylinder grows, its length (L) scales linearly with the aggregation number (α), and thus the distance from the edge of the cylinder to the center $\|r_i(\theta,\psi) - r_0\|$ from eqn (3) increases. However, given that the radius of the cylinder remains constant, the value of $\min(\{\|r_i(\theta,\psi) - r_0\|\})$ is also constant. This means that Ω must increase with an increase in α. Numerically, the relationship between Ω and α is computed by constructing a new surface mesh for cylinders at various lengths and then

evaluating eqn (3) at the relevant edge points associated with the growing front (Fig. 4e). This results in the following scaling relationship: $\Omega \sim \Omega_0\alpha^{1/2}$, where Ω_0 is a reference value for a given surface location in the limit of a unit cylinder (Fig. 4d and e).

To address the chain length constraints, we first note that the monomer density profile $\rho(r)$ in the long chain limit can be obtained by enforcing that the local monomer density inside the thermal correlation blob at a given subregion of the brush must be equal to the global monomer density across the entire particle surface, that is, equivalence between the loc and global density. In the long chain limit, the monomer density is assumed to exhibit good solvent behavior given that the chains are long enough to experience solvent penetration.[67] In the limit of intermediate and short chain lengths, analogous density profiles can be defined by imposing the semi-dilute and concentrate (poor) solvent behaviors within the thermal correlation blob.[51,67] Performing the local and global density balance with these solvent constraints yields the intermediate (eqn (4)) and short (eqn (5)) chain variants of the monomer density profile as follows:

$$\psi(r) \sim \Omega^{-3/2}\alpha^{1/2}\left(\frac{r}{b}\right)^{-1} \tag{4}$$

$$\psi(r) \sim 1 \tag{5}$$

Applying the same volumetric balance, $N\alpha b^3 \sim \int_0^{R(\Omega)} \rho(r)\Omega^3 r^2 \mathrm{d}r$, for each respective region and solving for R yield the brush size for intermediate chains (eqn (6)) and short chains (eqn (7)) as follows:

$$R_{\text{intermediate}} \sim \alpha^{1/4}N_{\text{f}}^{1/2}\Omega^{-3/4}b \tag{6}$$

$$R_{\text{short}} \sim \alpha^{1/3}N_{\text{f}}^{1/3}\Omega^{-1}b \tag{7}$$

where N_{f} is the chain length of the flexible block. To specialize eqn (6) and (7) to the cylindrical geometry of the core, we substitute in $\Omega \sim \Omega_0\alpha^{1/2}$ (Fig. 4e) to get the following:

$$R_{\text{intermediate}} \sim \alpha^{-1/8}N_{\text{f}}^{1/2}\Omega_0^{-3/4}b \tag{8}$$

$$R_{\text{short}} \sim \alpha^{-1/6}N_{\text{f}}^{1/3}\Omega_0^{-1}b \tag{9}$$

Eqn (8) and (9) enable direct quantification of the entropic penalty ($F_{\text{s}} \sim \nu\alpha N^2 R^{-3}$) due to steric repulsion between neighboring chains. Each amphiphile added to the growing assembly also provides an enthalpic gain of (F_{a}) from π–π stacking, which we define to be $F_{\text{a}} \sim -\varepsilon\alpha$, where ε is the total enthalpy change per amphiphile. The total free energy is thus $F = F_{\text{s}} + F_{\text{a}}$. We then solve for the equilibrium aggregation number (α^*) by taking $\dfrac{\mathrm{d}F}{\mathrm{d}\alpha} = 0$ to obtain the following scaling predictions for intermediate and short chains:

$$\alpha^*_{\text{intermediate}} \sim \varepsilon^{8/3}N_{\text{f}}^{-4/3} \tag{10}$$

$$\alpha^*_{\text{short}} \sim \varepsilon^2 N_{\text{f}}^{-2} \tag{11}$$

Measurements of the equilibrium aggregation number from simulation for comparison with theory prediction yield excellent agreement, as shown in Fig. 5a.

Note that the case of $N_{\text{c}} = 4$ utilizes short chain scaling (eqn (7)). This is because the longer conjugate blocks self-assemble into larger cores. This makes the relative size of the flexible block effectively shorter compared against the larger core, pushing behaviors into the short chain regime.

Along this vein, the boundary between intermediate versus short chain scaling can be defined by equating $R_{\text{intermediate}}$ and R_{short} to give $N_{\text{f}} \sim \alpha\Omega^{-3/2}$. Defining the effective surface coverage as $\lambda \sim \alpha r_0^{-2}$, where r_0 is the size of the core and plugging in for α yields $N_{\text{f}} \sim \lambda r_0^2\Omega^{-3/2}$. More specifically, the short chain limit should be used when $N_{\text{f}} < \lambda r_0^2\Omega^{-3/2}$ and the intermediate chain limit should be deployed when $N_{\text{f}} > \lambda r_0^2\Omega^{-3/2}$. By inspection, this means that a larger core requires a higher N_{f} before transition from the short to intermediate chain limit, which matches the need to use the short chain scaling (eqn (6)) for amphiphiles with a longer conjugated block length ($N_{\text{c}} = 4$).
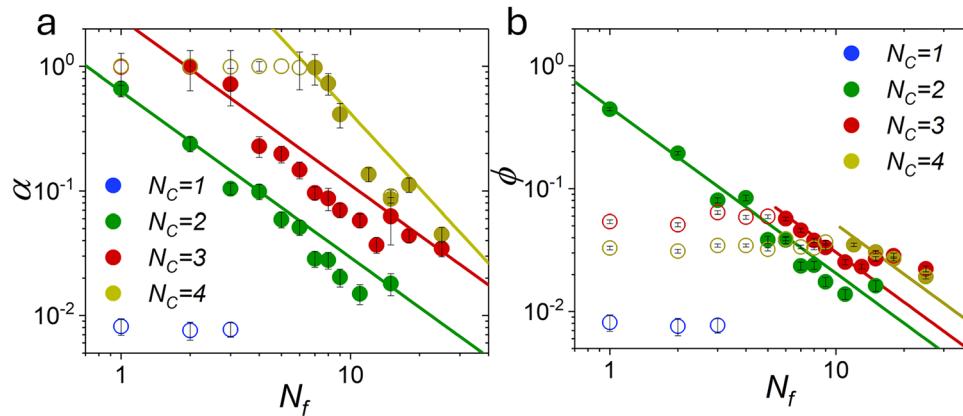

Fig. 5 Scaling prediction of self-limiting and assembly behaviors. Scaling behaviors of (a) α and (b) ϕ as a function of the flexible block length (N_f) for systems with N_c = 1, 2, 3, and 4 on a log–log axis. Solid lines represent theoretical predictions and scatters are measured from simulations. Scatter color corresponds to systems of different conjugated block lengths (N_c). Open scatter symbols represent systems in the network regime, and closed scatter symbols correspond to systems in the self-limiting regime. Comparison of the scaling prediction with the simulation results from the self-limiting regime shows excellent agreement across the set of amphiphiles studied. Error bars are standard error of the mean computed from averaging clusters from 3 different replicates for each system.

As discussed earlier, the stacking order parameter (ϕ) measures the degree of orientational alignment between the conjugated blocks. High alignment corresponds to tighter packing between neighboring amphiphiles, and thus a smaller effective corona size (flexible block) around the core. Conversely, low alignment correlates with highly branched networks, which increase the space taken up by the corona. These shifts alter the effective area available on the surface of the core formed *via* the assembled conjugated blocks. As a result, we expect $\phi \sim R^{-2}$ to hold, where R^2 defines the surface area. Combining eqn (8)–(11) with the above-mentioned scaling for ϕ yields:

$$\phi \sim N_f^{-4/3} \tag{12}$$

for both the short and intermediate chain limit. The developed scaling predictions (eqn (8)–(12)) focus on the behaviors for the self-limiting regime of amphiphile self-assembly. Direct comparison with simulations for systems exhibiting self-limiting behaviors (solid symbols, Fig. 5b) reveals excellent agreement with theory. We note that the plateau region in Fig. 5b (open symbols) arises due to network formation, and thus does not exhibit the scaling regimes predicted by eqn (8)–(12).

Morphology phase diagram

Based on the identified classes of morphologies suggested by the α_i and ϕ_i distributions (Fig. 3), we additionally define a classification in the α–ϕ plane, as shown in Fig. 6a. The morphologies are categorized into four classes, *i.e.*, no assembly (NA), self-limiting, filaments, and network, to match each of the four features observed, respectively (Fig. 3). NA corresponds to minimal associations between the amphiphiles. Accordingly, no assembly structures are observed in the simulation. This means that the normalized aggregation number is small and no alignments exist between the conjugated blocks. Therefore, we use $\alpha < 0.03$ to delineate the NA class. This cutoff value of 0.03 for α correlates with 97% of the amphiphiles in the simulation being dispersed and unassociated with other amphiphiles, which reflects the no assembly nature of the morphology characterization. Conversely, a network structure represents a highly crosslinked system. Here, we expect a high normalized aggregation number but a low degree of alignment between the conjugated blocks. This is because misaligned conjugated blocks can serve as branching sites for the growing structures, producing network morphologies. Thus, we define the boundary for the network structure as $\alpha > 0.5$ and $\phi < 0.5\alpha$. The first constraint reflects the idea that the majority of amphiphiles must belong to the same cluster to be considered a network. The second constraint ensures that more than 50% of the amphiphiles within the clusters have misaligned conjugated cores to delineate from filaments. Filaments exhibit long, fiber-like structures, where there is strong alignment between the aggregated conjugated blocks. However, due to their constrained growth along a singlet direction, the normalized aggregation number is bound by the alignment order parameter. This upper limit is due to the fact that the number of perfectly aligned amphiphiles within the self-assembled structure cannot exceed the number of amphiphiles within the filament. For this reason, we define the boundary for the filament structure as $0.1 < \alpha < 2\phi$, where the augmented upper bound was selected to account for fluctuations and artifacts arising from thermal noise/clustering that can lower the measured aggregation number from the associating amphiphiles. Lastly, the self-limiting morphology is characterized by large, singlet peaks in both α and ϕ to indicate that small aggregates are present, but no large-scale structures are observed in the simulations. However, the exact peak locations depend on the cluster size, and no set values can be defined. Thus, all remaining regions of the α–ϕ phase space not defined as NA, filament, or network are categorized as self-limiting.

Employing the above-mentioned classification across all simulations yields a phase diagram in the N_c *vs.* N_f plane, as shown in Fig. 6b (scatter points). Based on the defined classification, for the $N_c = 2$ system, filament-structures are observed when $N_f \leq 4$. Increasing N_f to be greater than 4 while keeping N_c the same ($N_c = 2$) produces a systematic transition to first self-limiting, and eventually no-assembly due to the increasingly larger entropic crowding between the flexible blocks.
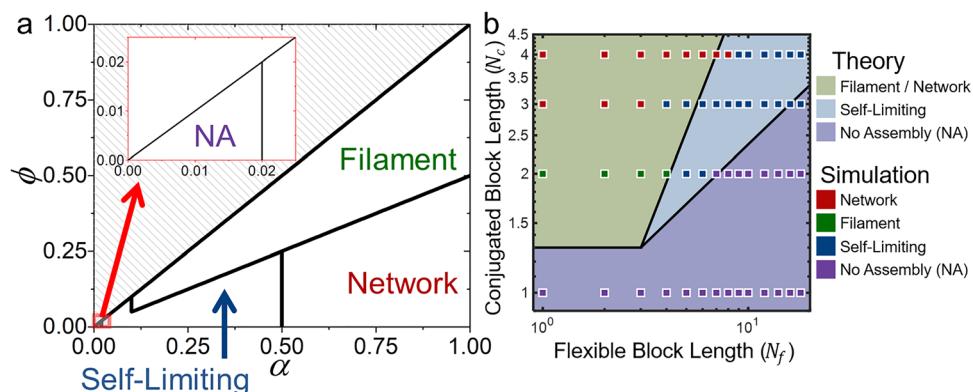
Fig. 6 Morphology phase diagram for the conjugated amphiphile self-assembly. (a) Phase diagram of α *versus* ϕ, showing the defined boundaries between different structural regimes used for categorization. (b) Phase diagram of self-assembled morphologies for conjugated peptide systems as a function of N_f and N_c. Simulation data are shown as scatter points. Theoretical predictions are shown in solid phases with predicted phase boundaries (eqn (13) and (14)) presented as solid lines.

Specifically, at N_f = 5 and 6, the system enters the self-limiting regime and $N_f > 6$ leads to a transition into the NA regime. In the N_c = 3 system, a network structure is observed when $N_f \leq 3$. As N_f increases, the system transitions into the small cluster regime. For N_c = 4, the boundary of the network regime extends to N_f = 8, beyond which the system again transitions into the small cluster regime.

To connect the phase classification from simulations to scaling theory predictions (eqn (8)–(12)), we additionally derive the phase boundary for the different morphological classes. In the case of NA, no assembly is observed. Thus, we expect $\alpha \rightarrow 1$ (only one amphiphile). Furthermore, we assume that each monomer within the conjugated block yields an identical increase in enthalpic gain in the growing assembly, that is, $\varepsilon \sim \varepsilon_0 N_c$, where ε_0 is the per monomer interaction energy and N_c is the length of the conjugated block. Plugging $\varepsilon \sim \varepsilon_0 N_c$ and setting the left-hand side of eqn (6) to 1 yield the crossover boundary as follows:

$$N_c \sim N_f^{1/2} \qquad (13)$$

Transitions from the self-limiting behaviors defined by eqn (6) to a network structure necessitates that the aggregation number approaches the upper limit bounded by phase separation between the conjugated and flexible blocks. This means that α must converge to the volume (V_c) occupied by the conjugated block in a concentrated (segregated) limit, as follows: $\alpha_{network} \sim V_c$. Given that the conjugated block is rigid, one direction (R_l) must be linear in $R_l \sim N_c$. The other two directions (R_p) simply reflect the packing scaling limit $R_p \sim N_c^{1/3}$. Combining them, we get $\alpha_{network} \sim V_c \sim R_l R_p^2 \sim N_c^{5/3}$. Setting $\alpha \sim \alpha_{network}$ in eqn (6) and solving for N_c yields:

$$N_c \sim N_f^{4/3} \qquad (14)$$

as the boundary between network/filament and self-limiting formation. The predicted phase boundaries from eqn (13) and (14) are also plotted in Fig. 6b in black lines, with colored regions corresponding to the regions bound by the phase boundary intersections. The results exhibit excellent agreement with the simulations. Together, our findings highlight a high degree of morphological diversity in flexible-conjugated-flexible amphiphiles, where the mesoscale assembly behaviors and local control over the spatial and orientational ordering of the conjugated domains can both be precisely tuned *via* simple manipulations of the length of individual blocks.

However, despite the agreement between theory and simulations, there are limitations in the scaling theory that should also be properly highlighted. Firstly, the proposed scaling theory assumes concentrations below the overlap concentrations between the self-assembled structures. High concentrations can induce corona interpenetration between the flexible blocks, which can drive hierarchical organization between the filaments. These effects were not explicitly considered in our scaling derivations. Additionally, given that we directly plugged in $\Omega \sim \Omega_0 \alpha^{1/2}$ as the scaling behavior for Ω with respect to the aggregation number, eqn (8)–(14) are only valid for cylindrical cores. Generalization to other core geometries will necessitate defining different scaling exponents for how Ω changes with an increase in the aggregation number (α). Finally, an implicit assumption in computing the monomer density profiles for both short and intermediate chain lengths (eqn (4) and (5)) is that the interactions between monomers making up the flexible blocks are sterically repulsive. Also, more complex features such as chain–chain attraction/repulsion are not captured by the developed scaling theory.

IV. Conclusion

In summary, we employ molecular dynamics simulations to study the assembly behaviors of amphiphiles with a flexible-conjugate-flexible triblock architecture. Firstly, we develop a coarse-grained model for simulating the conjugated blocks that explicitly retain the underlying geometry of the conjugated monomers, thereby enabling characterization of how local stackings directed by the monomer shape dictate the mesoscale assembly behaviors. Then, we show how shifts in experimentally relevant handles such as flexible and conjugate block lengths can alter the emergent self-assembled morphologies. To elucidate the physical origins of how each design handle sculpts the subsequent self-assembly, we employ the polymer brush scaling theory to predict trends in both the equilibrium aggregation number and orientational ordering between the conjugated blocks. We further employ theory to predict the phase boundaries between the different classes of mesoscale structures, including filaments, network, self-limiting, and disorder, accessible to this class of amphiphile architecture, providing a computationally validated morphology phase diagram to guide experimental synthesis. Our work not only provides a new approach to simulating conjugated amphiphiles at the mesoscale but also elucidates the underlying mechanism of how shifts in experimentally relevant amphiphile design parameters can sculpt emergent assembly behaviors. The former provides a critical step forward to enable the large-scale simulations of conjugated amphiphiles, while the latter provides key fundamental insights into the microscopic forces governing supramolecular assembly behaviors.

Author contributions

X. Z. carried out the simulations and performed the analysis. T. V. developed theory and directed the research. All the authors contributed to data analysis and the writing of the manuscript.

Conflicts of interest

The authors declare no conflicts of interest.

Data availability

Numerical data and results for the structural analysis and characterizations presented in the main text are provided in the accompanying ZIP file with the sample analysis scripts. Sample simulation scripts to perform MD simulations are also included in the ZIP file. These analysis and simulation scripts reproduce the data shown in all the figures of the main text. Additionally, a sample simulation dataset (GSD file format) is provided representing the results obtained from running the included scripts. All codes are available on our repository: https://github.com/VoGroupJHU/Conjugated_Amphiphile.

Acknowledgements

References

1 C. M. Bates and F. S. Bates, 50th Anniversary Perspective: Block Polymers-Pure Potential, *Macromolecules*, 2017, **50**(1), 3–22, DOI: **10.1021/ACS.MACROMOL.6B02355**.

2 T. Pan, S. Dutta, Y. Kamble, B. B. Patel, M. A. Wade, S. A. Rogers, Y. Diao, D. Guironnet and C. E. Sing, Materials Design of Highly Branched Bottlebrush Polymers at the Intersection of Modeling, Synthesis, Processing, and Characterization, *Chem. Mater.*, 2022, **34**(5), 1990–2024, DOI: **10.1021/ACS.CHEMMATER.1C04030**.

3 K. Chen, X. Hu, N. Zhu, K. K. Guo Chen, N. Zhu, K. Guo, K. Chen and X. Hu, Design, Synthesis, and Self-Assembly of Janus Bottlebrush Polymers, *Macromol. Rapid Commun.*, 2020, **41**(20), 2000357, DOI: **10.1002/MARC.202000357**.

4 K. H. Kim, J. Nam, J. Choi, M. Seo and J. Bang, From Macromonomers to Bottlebrush Copolymers with Sequence Control: Synthesis, Properties, and Applications, *Polym. Chem.*, 2022, **13**(16), 2224–2261, DOI: **10.1039/D2PY00126H**.

5 A. L. Ferguson and J. D. Tovar, Evolution of π-Peptide Self-Assembly: From Understanding to Prediction and Control, *Langmuir*, 2022, **38**(50), 15463–15475, DOI: **10.1021/ACS.LANGMUIR.2C02399**.

6 K. C. Yang, D. M. Rivera Mirabal, R. V. Garcia, N. W. Vlahakis, P. H. Nguyen, S. D. Mengel, M. Mecklenburg, J. A. Rodriguez, M. S. Shell, C. J. Hawker and R. A. Segalman, Crystallization-Induced Flower-like Superstructures via Peptoid Helix Assembly, *ACS Macro Lett.*, 2024, 423–428, DOI: **10.1021/ACSMACROLETT.4C00039**.

7 T. M. Swager, 50th Anniversary Perspective: Conducting/Semiconducting Conjugated Polymers. A Personal Perspective on the Past and the Future, *Macromolecules*, 2017, **50**(13), 4867–4886, DOI: **10.1021/ACS.MACROMOL.7B00582**.

8 C. A. Mirkin and S. H. Petrosko, Inspired Beyond Nature: Three Decades of Spherical Nucleic Acids and Colloidal Crystal Engineering with DNA, *ACS Nano*, 2023, **17**(17), 16291–16307, DOI: **10.1021/acsnano.3c06564**.

9 J. S. Kahn and O. Gang, Designer Nanomaterials through Programmable Assembly, *Angew. Chem., Int. Ed.*, 2022, **61**(3), e202105678, DOI: **10.1002/ANIE.202105678**.

10 M. A. Boles, M. Engel and D. V. Talapin, Self-Assembly of Colloidal Nanocrystals: From Intricate Structures to Functional Materials, *Chem. Rev.*, 2016, **116**(18), 11220–11289, DOI: **10.1021/ACS.CHEMREV.6B00196**.

11 T. Li, X. M. Lu, M. R. Zhang, K. Hu and Z. Li, Peptide-Based Nanomaterials: Self-Assembly, Properties and Applications, *Bioact. Mater.*, 2022, **11**, 268–282, DOI: **10.1016/J.BIOACTMAT.2021.09.029**.

12 Z. Li, Q. Fan and Y. Yin, Colloidal Self-Assembly Approaches to Smart Nanostructured Materials, *Chem. Rev.*, 2022, **122**(5), 4976–5067, DOI: **10.1021/ACS.CHEMREV.1C00482**.

13 T. Vo, Patchy Nanoparticles with Surface Complexity for Directed Self-Assembly, *MRS Bull.*, 2024, **49**(4), 330–339, DOI: **10.1557/s43577-024-00687-9**.

14 S. Kang, G. H. Kim and S. J. Park, Conjugated Block Copolymers for Functional Nanostructures, *Acc. Chem. Res.*, 2022, **55**(16), 2224–2234, DOI: **10.1021/ACS.ACCOUNTS.2C00244**.

15 L. R. MacFarlane, H. Shaikh, J. D. Garcia-Hernandez, M. Vespa, T. Fukui and I. Manners, Functional Nanoparticles through π-Conjugated Polymer Self-Assembly, *Nat. Rev. Mater.*, 2020, **6**(1), 7–26, DOI: **10.1038/s41578-020-00233-4**.

16 S. Wang, G. Zuo, J. Kim and H. Sirringhaus, Progress of Conjugated Polymers as Emerging Thermoelectric Materials, *Prog. Polym. Sci.*, 2022, **129**, 101548, DOI: **10.1016/J.PROGPOLYMSCI.2022.101548**.

17 Z. Su, R. Zhang, X. Y. Yan, Q. Y. Guo, J. Huang, W. Shan, Y. Liu, T. Liu, M. Huang and S. Z. D. Cheng, The Role of Architectural Engineering in Macromolecular Self-Assemblies via Non-Covalent Interactions: A Molecular LEGO Approach, *Prog. Polym. Sci.*, 2020, **103**, 101230, DOI: **10.1016/J.PROGPOLYMSCI.2020.101230**.

18 R. Verduzco, X. Li, S. L. Pesek and G. E. Stein, Structure, Function, Self-Assembly, and Applications of Bottlebrush Copolymers, *Chem. Soc. Rev.*, 2015, **44**(8), 2405–2420, DOI: **10.1039/C4CS00329B**.

19 Z. Li, M. Tang, S. Liang, M. Zhang, G. M. Biesold, Y. He, S. M. Hao, W. Choi, Y. Liu, J. Peng and Z. Lin, Bottlebrush Polymers: From Controlled Synthesis, Self-Assembly, Properties to Applications, *Prog. Polym. Sci.*, 2021, **116**, 101387, DOI: **10.1016/J.PROGPOLYMSCI.2021.101387**.

20 Y. Zhu, W. Zheng, W. Wang and H. B. Yang, When Polymerization Meets Coordination-Driven Self-Assembly: Metallo-Supramolecular Polymers Based on Supramolecular Coordination Complexes, *Chem. Soc. Rev.*, 2021, **50**(13), 7395–7417, DOI: **10.1039/D0CS00654H**.

21 E. Elacqua, K. B. Manning, D. S. Lye, S. K. Pomarico, F. Morgia and M. Weck, Supramolecular Multiblock Copolymers Featuring Complex Secondary Structures, *J. Am. Chem. Soc.*, 2017, **139**(35), 12240–12250, DOI: **10.1021/JACS.7B06201**.

22 G. Polymeropoulos, G. Zapsas, K. Ntetsikas, P. Bilalis, Y. Gnanou and N. Hadjichristidis, 50th Anniversary Perspective: Polymers with Complex Architectures, *Macromolecules*, 2017, **50**(4), 1253–1290, DOI: **10.1021/ACS.MACROMOL.6B02569**.

23 K. Yue, M. Huang, R. L. Marson, J. Hec, J. Huang, Z. Zhou, J. Wang, C. Liu, X. Yan, K. Wu, Z. Guo, H. Liu, W. Zhang, P. Ni, C. Wesdemiotis, W. B. Zhang, S. C. Glotzer and S. Z. D. Cheng, Geometry Induced Sequence of Nanoscale Frank-Kasper and Quasicrystal Mesophases in Giant Surfactants, *Proc. Natl. Acad. Sci. U. S. A.*, 2016, **113**(50), 14195–14200, DOI: **10.1073/PNAS.1609422113**.

24 Q. Shi, Z. Zhang and S. Liu, Precision Sequence-Defined Polymers: From Sequencing to Biological Functions, *Angew. Chem., Int. Ed.*, 2023, **2023**, e202313370, DOI: **10.1002/ANIE.202313370**.

25 M. J. Austin and A. M. Rosales, Tunable Biomaterials from Synthetic, Sequence-Controlled Polymers, *Biomater. Sci.*, 2019, **7**(2), 490–505, DOI: **10.1039/C8BM01215F**.

26 S. Martens, J. O. Holloway, F. E. Du Prez, S. Martens, J. O. Holloway and F. E. Du Prez, Click and Click-Inspired Chemistry for the Design of Sequence-Controlled Polymers, *Macromol. Rapid Commun.*, 2017, **38**(24), 1700469, DOI: **10.1002/MARC.201700469**.

27 A. S. Knight, E. Y. Zhou, M. B. Francis, R. N. Zuckermann, A. S. Knight, E. Y. Zhou, M. B. Francis and R. N. Zuckermann, Sequence Programmable Peptoid Polymers for Diverse Materials Applications, *Adv. Mater.*, 2015, **27**(38), 5665–5691, DOI: **10.1002/ADMA.201500275**.

28 X. Feng, R. Zhang, Y. Li, Y. L. Hong, D. Guo, K. Lang, K. Y. Wu, M. Huang, J. Mao, C. Wesdemiotis, Y. Nishiyama, W. Zhang, T. Miyoshi, T. Li and S. Z. D. Cheng, Hierarchical Self-Organization of ABn Dendron-like Molecules into a Supramolecular Lattice Sequence, *ACS Cent. Sci.*, 2017, **3**(8), 860–867, DOI: **10.1021/ACSCENTSCI.7B00188**.

29 Z.-L. Li, F.-R. Zeng, J.-M. Ma, L.-H. Sun, Z. Zeng, H. Jiang, Z. Li, F. Zeng, J. Ma, L. Sun, Z. Zeng and H. Jiang, Precision Aliphatic Polyesters with Alternating Microstructures via Cross-Metathesis Polymerization: An Event of Sequence Control, *Macromol. Rapid Commun.*, 2017, **38**(12), 1700050, DOI: **10.1002/MARC.201700050**.

30 G. H. Gelinck, H. E. A. Huitema, E. Van Veenendaal, E. Cantatore, L. Schrijnemakers, J. B. P. H. Van Der Putten, T. C. T. Geuns, M. Beenhakkers, J. B. Giesbers, B. H. Huisman, E. J. Meijer, E. M. Benito, F. J. Touwslager, A. W. Marsman, B. J. E. Van Rens and D. M. De Leeuw, Flexible Active-Matrix Displays and Shift Registers Based on Solution-Processed Organic Transistors, *Nat. Mater.*, 2004, **3**, 106–110, DOI: **10.1038/nmat1061**.

31 E. C. P. Smits, S. G. J. Mathijssen, P. A. Van Hal, S. Setayesh, T. C. T. Geuns, K. A. H. A. Mutsaers, E. Cantatore, H. J. Wondergem, O. Werzer, R. Resel, M. Kemerink, S. Kirchmeyer, A. M. Muzafarov, S. A. Ponomarenko, B. De Boer, P. W. M. Blom and D. M. De Leeuw, Bottom-up Organic Integrated Circuits, *Nature*, 2008, **455**(7215), 956–959, DOI: **10.1038/nature07320**.

32 D. Yang and D. Ma, Development of Organic Semiconductor Photodetectors: From Mechanism to Applications, *Adv. Opt. Mater.*, 2019, **7**, 1800522, DOI: **10.1002/adom.201800522**.

33 J. A. Olive, M. D. Behn, G. Ito, W. R. Buck, J. Escartín and S. Howell, Sensitivity of Seafloor Bathymetry to Climate-Driven Fluctuations in Mid-Ocean Ridge Magma Supply, *Science*, 2015, **350**(6258), 310–313, DOI: **10.1126/science.aad0715**.

34 W. Gao, H. Ota, D. Kiriya, K. Takei and A. Javey, Flexible Electronics toward Wearable Sensing, *Acc. Chem. Res.*, 2019, **52**(3), 523–533, DOI: **10.1021/ACS.ACCOUNTS.8B00500**.

35 H. Wang, Z. Li, Z. Liu, J. Fu, T. Shan, X. Yang, Q. Lei, Y. Yang and D. Li, Flexible Capacitive Pressure Sensors for Wearable Electronics, *J. Mater. Chem. C*, 2022, **10**(5), 1594–1605, DOI: **10.1039/D1TC05304C**.

36 I. Aazem, D. T. Mathew, S. Radhakrishnan, K. V. Vijoy, H. John, D. M. Mulvihill and S. C. Pillai, Electrode Materials for Stretchable Triboelectric Nanogenerator in Wearable Electronics, *RSC Adv.*, 2022, **12**(17), 10545–10572, DOI: **10.1039/D2RA01088G**.

37 G. H. Lee, H. Moon, H. Kim, G. H. Lee, W. Kwon, S. Yoo, D. Myung, S. H. Yun, Z. Bao and S. K. Hahn, Multifunctional Materials for Implantable and Wearable Photonic Healthcare Devices, *Nat. Rev. Mater.*, 2020, **5**(2), 149–165, DOI: **10.1038/s41578-019-0167-3**.

38 P. C. Y. Chow, T. Someya, P. C. Y. Chow and T. Someya, Organic Photodetectors for Next-Generation Wearable Electronics, *Adv. Mater.*, 2020, **32**(15), 1902045, DOI: **10.1002/ADMA.201902045**.

39 H. Su, F. Wang, H. Wang, W. Zhang, C. F. Anderson and H. Cui, Propagation-Instigated Self-Limiting Polymerization of Multiarmed Amphiphiles into Finite Supramolecular Polymers, *J. Am. Chem. Soc.*, 2021, **143**(44), 18446–18453, DOI: **10.1021/JACS.1C06495**.

40 A. Vidyasagar, S. H. Ku, M. Kim, M. Kim, H. S. Lee, T. R. Pearce, A. V. McCormick, F. S. Bates and E. Kokkoli, Design and Characterization of a PVLA-PEG-PVLA Thermosensitive and Biodegradable Hydrogel, *ACS Macro Lett.*, 2017, **6**(10), 1134–1139, DOI: **10.1021/ACSMACROLETT.7B00523**.

41 S. S. Panda, K. Shmilovich, N. S. M. Herringer, N. Marin, A. L. Ferguson and J. D. Tovar, Computationally Guided Tuning of Peptide-Conjugated Perylene Diimide Self-Assembly, *Langmuir*, 2021, **37**(28), 8594–8606, DOI: **10.1021/ACS.LANGMUIR.1C01213**.

42 A. C. Kamps, M. H. M. Cativo, M. Fryd and S. J. Park, Self-Assembly of Amphiphilic Conjugated Diblock Copolymers into One-Dimensional Nanoribbons, *Macromolecules*, 2014, **47**(1), 161–164, DOI: **10.1021/MA4021483**.

43 K. Shmilovich, Y. Yao, J. D. Tovar, H. E. Katz, A. Schleife and A. L. Ferguson, Computational Discovery of High Charge Mobility Self-Assembling π-Conjugated Peptides, *Mol. Syst. Des. Eng.*, 2022, **7**(5), 447–459, DOI: **10.1039/D2ME00017B**.

44 I. H. Lee, P. Amaladass, K. Y. Yoon, S. Shin, Y. J. Kim, I. Kim, E. Lee and T. L. Choi, Nanostar and Nanonetwork Crystals Fabricated by in Situ Nanoparticlization of Fully Conjugated Polythiophene Diblock Copolymers, *J. Am. Chem. Soc.*, 2013, **135**(47), 17695–17698, DOI: **10.1021/JA409206P**.

45 M. Misra, Z. Liu, B. X. Dong, S. N. Patel, P. F. Nealey, C. K. Ober and F. A. Escobedo, Thermal Stability of π-Conjugated n-Ethylene-Glycol-Terminated Quaterthiophene Oligomers: A Computational and Experimental Study, *ACS Macro Lett.*, 2020, **9**(3), 295–300, DOI: **10.1021/acsmacrolett.9b00935**.

46 R. Gupta, M. Misra, W. Zhang, A. Mukhtyar, S. P. Gido, A. Ribbe, F. A. Escobedo and E. B. Coughlin, Topological Frustration as a New Parameter to Tune Morphology

Revealed through Exploring the Continuum between A-B-C 3-Arm Star and Linear Triblock Polymers, *Macromolecules*, 2021, **54**(9), 4401–4411, DOI: **10.1021/acs.macromol.1c00277**.

47 S. S. Panda and J. D. Tovar, Aqueous Self-Assembly of Peptide–Diketopyrrolopyrrole Conjugates with Variation of N-Alkyl Side Chain and π-Core Lengths, *Org. Mater.*, 2021, **03**(02), 353–361, DOI: **10.1055/A-1503-5912**.

48 G. Grover, J. D. Tovar and M. Kertesz, Quinonoid versus Aromatic π-Conjugated Oligomers and Polymers and Their Diradical Characters, *J. Phys. Chem. C*, 2022, **126**(11), 5302–5310, DOI: **10.1021/ACS.JPCC.2C00113**.

49 W. Zhang, F. Wang, H. Wang, T. Xu, H. Su and H. Cui, Balancing Chemical and Supramolecular Stability in OEGylated Supramolecular Polymers for Systemic Drug Delivery, *J. Am. Chem. Soc.*, 2025, **147**(21), 17985–17993, DOI: **10.1021/jacs.5c03253**.

50 H. Cui and M. Tirrell, Self-Assembling Peptides, Conjugates, and Mimics: A Versatile Platform for Materials and Beyond, *Acc. Chem. Res.*, 2025, **58**(2), 163–164, DOI: **10.1021/acs.accounts.4c00805**.

51 T. Vo, Theory and Simulation of Ligand Functionalized Nanoparticles – a Pedagogical Overview, *Soft Matter*, 2024, **20**(17), 3554–3576, DOI: **10.1039/D4SM00177J**.

52 T. Vo and S. C. Glotzer, Principle of Corresponding States for Hard Polyhedron Fluids, *Mol. Phys.*, 2019, **117**(23–24), 3518–3526, DOI: **10.1080/00268976.2019.1640906**.

53 K. Akkunuri, X. Zhang and T. Vo, Elucidating the Interplay between Entropy-Driven and Patch-Mediated Bonding in Directing Nanoscale Assemblies, *Mol. Syst. Des. Eng.*, 2024, **10**(1), 19–31, DOI: **10.1039/D4ME00153B**.

54 A. Kim, K. Akkunuri, C. Qian, L. Yao, K. Sun, Z. Chen, T. Vo and Q. Chen, Direct Imaging of "Patch-Clasping" and Relaxation in Robust and Flexible Nanoparticle Assemblies, *ACS Nano*, 2024, **18**(1), 939–950, DOI: **10.1021/acsnano.3c09710**.

55 S. S. Panda, K. Shmilovich, A. L. Ferguson and J. D. Tovar, Computationally Guided Tuning of Amino Acid Configuration Influences the Chiroptical Properties of Supramolecular Peptide-π-Peptide Nanostructures, *Langmuir*, 2020, **36**(24), 6782–6792, DOI: **10.1021/ACS.LANGMUIR.0C00961**.

56 E. R. Jira, K. Shmilovich, T. S. Kale, A. Ferguson, J. D. Tovar and C. M. Schroeder, Effect of Core Oligomer Length on the Phase Behavior and Assembly of π-Conjugated Peptides, *ACS Appl. Mater. Interfaces*, 2020, **12**(18), 20722–20732, DOI: **10.1021/ACSAMI.0C02095**.

57 S. J. Marrink, H. J. Risselada, S. Yefimov, D. P. Tieleman and A. H. De Vries, The MARTINI Force Field: Coarse Grained Model for Biomolecular Simulations, *J. Phys. Chem. B*, 2007, **111**(27), 7812–7824, DOI: **10.1021/JP071097F**.

58 P. Vainikka, S. Thallmair, P. C. T. Souza and S. J. Marrink, Martini 3 Coarse-Grained Model for Type III Deep Eutectic Solvents: Thermodynamic, Structural, and Extraction Properties, *ACS Sustainable Chem. Eng.*, 2021, **9**(51), 17338–17350, DOI: **10.1021/ACSSUSCHEMENG.1C06521**.

59 E. Lee, B. Hammer, J. K. Kim, Z. Page, T. Emrick and R. C. Hayward, Hierarchical Helical Assembly of Conjugated Poly(3-Hexylthiophene)-Block- Poly(3-Triethylene Glycol Thiophene) Diblock Copolymers, *J. Am. Chem. Soc.*, 2011, **133**(27), 10390–10393, DOI: **10.1021/JA2038547**.

60 J. Wilson, J. S. Dal Williams, C. Petkovsek, P. Reves, Jurss, N. I. Hammer, G. S. Tschumper and D. L. Watkins, Synergistic Effects of Halogen Bond and π–π Interactions in Thiophene-Based Building Blocks, *RSC Adv.*, 2015, **5**(100), 82544–82548, DOI: **10.1039/C5RA16680B**.

61 V. Ramasubramani, T. Vo, J. A. Anderson and S. C. Glotzer, A Mean-Field Approach to Simulating Anisotropic Particles, *J. Chem. Phys.*, 2020, **153**(8), 084106, DOI: **10.1063/5.0019735**.

62 J. D. Weeks, D. Chandler and H. C. Andersen, Role of Repulsive Forces in Determining the Equilibrium Structure of Simple Liquids, *J. Chem. Phys.*, 1971, **54**(12), 5237–5247, DOI: **10.1063/1.1674820**.

63 K. Kremer and G. S. Grest, Dynamics of Entangled Linear Polymer Melts: A Molecular-dynamics Simulation, *J. Chem. Phys.*, 1998, **92**(8), 5057, DOI: **10.1063/1.458541**.

64 E. K. Watkins and W. L. Jorgensen, Perfluoroalkanes: Conformational Analysis and Liquid-State Properties from Ab Initio and Monte Carlo Calculations, *J. Phys. Chem. A*, 2001, **105**(16), 4118–4125, DOI: **10.1021/jp004071w**.

65 J. A. Anderson, J. Glaser and S. C. Glotzer, HOOMD-Blue: A Python Package for High-Performance Molecular Dynamics and Hard Particle Monte Carlo Simulations, *Comput. Mater. Sci.*, 2020, **173**, 109363, DOI: **10.1016/J.COMMATSCI.2019.109363**.

66 W. G. Hoover, Canonical Dynamics: Equilibrium Phase-Space Distributions, *Phys. Rev. A:At., Mol., Opt. Phys.*, 1985, **31**(3), 1695–1697, DOI: **10.1103/PhysRevA.31.1695**.

67 F. Lu, T. Vo, Y. Zhang, A. Frenkel, K. G. Yager, S. Kumar and O. Gang, Unusual Packing of Soft-Shelled Nanocubes, *Sci. Adv.*, 2019, **5**(5), 2399–2416, DOI: **10.1126/SCIADV.AAW2399**.

68 K. C. Elbert, W. Zygmunt, T. Vo, C. M. Vara, D. J. Rosen, N. M. Krook, S. C. Glotzer and C. B. Murray, Anisotropic Nanocrystal Shape and Ligand Design for Co-Assembly, *Sci. Adv.*, 2021, **7**(23), eabf9402, DOI: **10.1126/SCIADV.ABF9402**.

69 K. C. Elbert, T. Vo, N. M. Krook, W. Zygmunt, J. Park, K. G. Yager, R. J. Composto, S. C. Glotzer and C. B. Murray, Dendrimer Ligand Directed Nanoplate Assembly, *ACS Nano*, 2019, **13**(12), 14241–14251, DOI: **10.1021/ACSNANO.9B07348**.

70 E. R. Jira, K. Shmilovich, T. S. Kale, A. Ferguson, J. D. Tovar and C. M. Schroeder, Effect of Core Oligomer Length on the Phase Behavior and Assembly of π-Conjugated Peptides, *ACS Appl. Mater. Interfaces*, 2020, **12**(18), 20722–20732, DOI: **10.1021/acsami.0c02095**.